www.czasopisma.pan.pl PAN POLSKA AKADEMIA NAUK www.journals.pan.pl

ARCHIVES OF ACOUSTICS Vol. 48, No. 1, pp. 25–38 (2023), doi: 10.24425/aoa.2023.144263

Research Paper

Numerical Simulation of Breast Cancer in the Early Diagnosis with Actual Dimension and Characteristics Using Photoacoustic Tomography

Maryam AHANGAR DARBAND(1), Esmaeil NAJAFI AGHDAM(1)*, Arash GHARIBI(2)

(1) *Department of Electrical Engineering, Sahand University of Technology*
Tabriz, Iran

(2) *Institute of Modern Physics, Shanxi Normal University*
Linfen, China

*Corresponding Author e-mail: najafiaghdam@sut.ac.ir

(*received August 26, 2021; accepted August 30, 2022*)

A numerical study and simulation of breast imaging in the early detection of tumors using the photoacoustic (PA) phenomenon are presented. There have been various reports on the simulation of the PA phenomenon in the breast, which are not in the real dimensions of the tissue. Furthermore, the different layers of the breast have not been considered. Therefore, it has not been possible to rely on the values and characteristics of the resulting data and to compare it with the actual state. Here, the real dimensions of the breast at three-dimensional and different constituent layers have been considered. After reviewing simulation methods and software for different stages of the PA phenomenon, a single suitable platform, which is commercially available finite element software (COMSOL), has been selected for simulating. The optical, thermal, elastic, and acoustic characteristics of different layers of breast and tumor at radiated laser wavelength (800 nm) were accurately calculated or obtained from a reliable source. Finally, by defining an array of 32 ultrasonic sensors on the breast cup at the defined arcs of the 2D slices, the PA waves can be collected and transmitted to MATLAB software to reconstruct the images. We can study the resulting PA wave and its changes in more detail using our scenarios.

Keywords: photoacoustic (PA); photoacoustic imaging (PAI); photoacoustic tomography; breast cancer; early diagnosis.

1. Introduction

Breast cancer is one of the most common forms of cancer among females, but it is less common among men. In 2019, the estimated 268,600 new cases of invasive breast cancer were diagnosed among women and approximately 2,670 cases were diagnosed in men. Breast cancer typically has no symptoms when the tumor is small and can be easily treated, therefore screening is vital for early detection (American Cancer Society, 2019). There are several methods for carefully screening breast tissue to identify cancerous tumors. However, a low-risk and non-invasive way that can detect cancerous tumors early is a priority. Among the available imaging modalities for breast tomography, we discuss the advantages and disadvantages of only two types of these methods in this paper which are based on pure optical and pure acoustic imaging. The photoacoustic (PA) approach combines these two methods and takes the best of both. The main limitation of the pure optical imaging modalities for breast cancer detection, such as diffuse optical tomography (DOT), fluorescence molecular tomography (FMT) (CORLU *et al.*, 2007), and optical coherence tomography (BOPPART *et al.*, 2004) is the scattering of light in the environment. It lowers the spatial resolution in deep tissue imaging. Light photons can penetrate to a depth of up to 1 mm of living tissue without scattering, as they are based on ballistic and quasi-ballistic photons (WANG, 2008). The scattering of ul-

trasonic waves in living tissue is approximately 2–3 orders of magnitude weaker than in optical waves; therefore, pure ultrasonic imaging has a better resolution than optical imaging. However, in pure acoustic imaging, the image's contrast is determined by the mechanical and elastic properties of the living tissue. Therefore, the contrast of the images may not be suitable for the early detection of a cancerous tumor (Wang, 2004). Photoacoustic imaging (PAI) has become an attractive, low-risk, and non-invasive tool in imaging biological tissues using non-ionized short laser pulse absorption and receiving PA signals. The PAI is based on the PA phenomenon discovered in 1880 by Alexander Graham Bell. It refers to the generation of acoustic waves by the absorption of electromagnetic energy such as optical or radiofrequency. The use of this phenomenon in medical imaging had not been formed before the advent of the laser light. To generate an acoustic pressure wave in the PA phenomenon, the temperature changes in the sample must be variable which can be achieved by the pulsed laser light or continuous laser light with the power intensity modulated at a constant or variable frequency. Due to the high signal-to-noise ratio of pulsed laser light, we use it in PAI, by considering the maximum permissible pulse energy and the maximum permissible pulse repetition rate governed by the American National Standards Institute (ANSI) laser safety standards. To use the PA phenomenon in tissue imaging and to obtain information about the density, sound speed, and geography of the tissue, a short (instead of long) homogenized pulsed laser light should be used (Wang, 2017). Then, by sampling information and signals of the ultrasonic detector and choosing appropriate image reconstruction algorithms, the tissue can be imaged. The use of PAI for breast tissue in the early diagnosis of breast tumors and cancer has been expanded in recent decades because it combines the high optical contrast of tissue chromophores and the high spatial resolution of pure ultrasonic imaging (Lin *et al.*, 2018). According to angiogenesis of breast cancer and subsequent mapping of endogenous breast chromophore concentration including oxy- (HbO_2) and deoxyhemoglobin (HHb), PAI could show high spatial resolution and sensitivity in the early detection of tumors, including dense breas (Laufer *et al.*, 2006). Additionally, tissue imaging using the PA phenomenon (Silverman *et al.*, 2010), especially in the early detection of cancerous tumors, has been extensively studied. It is also possible to detect and track different materials in various environments such as liquid and gas by using the PA phenomena (Pogorzelski *et al.*, 1999; Ponikwicki *et al.*, 2019).

2. Materials and methods

Following this section: we describe the different simulation software that we have used in various steps of the PA phenomenon and finally choose the most suitable simulation software. Later the governing equations of the PA phenomenon are briefly discussed. We show the simulated shape of tissue in our COMSOL simulation by expressing the actual structure of breast tissue and its different parts. Different modules of COMSOL software and their necessary parameters have also been stated by relevant mathematical relations. In addition, the image reconstruction method has been discussed using MATLAB code for the reconstruction of 2D tomographic image slices of breast tissue. The remaining sections concern the study of reports resulting from simulation.

2.1. Simulation of the photoacoustic phenomenon using different software

To have a risk-free environment and insight into dynamics, visualization, increasing accuracy, handling uncertainty, and saving money and time, we first decided to use PAI simulation modeling. There are some methods for simulating different parts of the PA phenomenon. In the following subsections, we briefly describe some of the techniques that we have used and choose the best one.

2.1.1. Software for modeling the homogenizing system of laser light

To transfer the laser energy uniformly to the 2D tomographic slices, in the 3D imaging process of the tissue, it is critical to shape and homogenize the laser light with suitable optical systems. For this purpose, various methods such as refractive, diffractive, and microlens (imaging and non-imaging) beam homogenizers (Ai *et al.*, 2017) are available for which VirtualLab Fusion has been used. This part of the simulation is essential in PA system building.

2.1.2. Simulation of light tissue interaction and PA generation and propagation

The Monte Carlo method is an approach used to solve forward modeling problems in many different fields of physics. It is also used to simulate how photons are transported and absorbed in turbid media. The Monte Carlo model of steady-state light transport in multilayered tissue (MCML) helps us determine the amount of light absorption in the studied tissue (Wang, Jacques, 1992; Jacques, Wang, 1995). After acquiring light tissue interaction data, for simulation of PA generation and propagation, we must import the absorption data matrix into the K-wave MATLAB toolbox and simulate the time-domain PA propagating for homogeneous or heterogeneous medium in one, two, and three dimensions (Treeby, Cox, 2010).

Furthermore, a finite element (FE) – based simulation model has been developed incorporating light propagation, PA signal generation, and sound wave prop-

agation, in soft tissues using a commercial FE simulation package, COMSOL Multiphysics. By using the simulation mentioned in the first part, MCML for light and tissue interaction, and K-wave MATLAB toolbox for photoacoustic propagation, the simulations are intermittent and incoherent. However, MCML is very time-consuming (Cassidy *et al.*, 2018; Wang *et al.*, 2012). In the case of MCML and K-wave toolbox, we cannot maneuver on the actual shape, size, and geometry of the tissue (Akhlaghi *et al.*, 2019). According to the above-mentioned reasons and the fact that the PA phenomena is multiphysics, it seems that the FEM should be a suitable option for this simulation. The FEM method is an efficient and accurate approach for PA phenomena simulation. Thus, we switch to a single platform, COMSOL, to carefully model and solve the problems expressed.

2.1.3. The final software selected for this research

This research has used commercially available finite element software (COMSOL) as a single platform for simulating PAI in the breast tissue. Based on the latest reports (Sowmiya, Thittai, 2017) concerning numerical modeling of PA, the tissue should be performed in tiny dimensions and an unrealistic shape to reduce the calculations and complexity of simulations. With regards to our modeling, the actual dimensions of breast tissue with its various components, including muscle, mammary glands, and fat, have been considered. Each stage of the PA signal generation process, including the effect of penetration of the radiant laser, the conversion of absorbed light into heat, the expansion of the tissue in volume and stress generation, and consequently mechanical expansion generating acoustic pressure wave propagating in the tissue would be fully modeled in COMSOL. Moreover, by changing the tumor location to different areas of breast tissue and its diameter, we maneuver the PA signal resulting from different conditions and positions. Besides all this, the arrangement of ultrasonic sensors is very similar to the real state. Finally, the PA signal obtained from an array of the detector on breast tissue in COMSOL software is converted into images by image reconstruction algorithm codes written in MATLAB.

2.2. A brief description of mathematical equations

Using linear fluid dynamics equations, a pair of coupled differential equations for temperature and pressure can be developed. According to Morse and Ingard, changes in temperature (T) and pressure (P) from their ambient values can be expressed as follows (Wang, 2017):

$$\frac{\partial}{\partial t}\left(T - \frac{\gamma - 1}{\gamma\alpha}P\right) = \frac{k}{\rho C_p}\nabla^2 T + \frac{H}{\rho C_p} \tag{1}$$

and

$$\left[\nabla^2 - \frac{\gamma}{v_s^2}\frac{\partial^2}{\partial t^2}\right]P = -\frac{\alpha\gamma}{v_s^2}\frac{\partial^2}{\partial t^2}T, \tag{2}$$

where γ is the specific heat ratio, α (pressure expansion coefficient) $= \left(\frac{\partial P(\text{pressure})}{\partial T(\text{temperature})}\right)_{V(\text{volume})}$, k is the thermal conductivity, C_p is the specific heat, p is the ambient density, v_s is the sound speed, t is the time, and H is the energy per unit volume and time deposited by the optical radiation beam (Wang, 2017).

The aforementioned equations did not include the effects of viscosity or energy relaxation. Assuming $\gamma = 1$, which for most fluids is a common and acceptable assumption, and assuming heat conductivity is set to zero ($\nabla T = 0$), then Eqs. (1) and (2) reduce to an equation for heat diffusion and a wave equation relating pressure to the speed of sound:

$$\left[\nabla^2 - \frac{1}{v_s^2}\frac{\partial^2}{\partial t^2}\right]p = -\frac{\beta}{C_p}\frac{\partial H}{\partial t}, \tag{3}$$

where $\beta = \left(\frac{1}{V}\right)\left(\frac{\partial V}{\partial T}\right)_p$ and $\alpha = \frac{\rho\beta v_s^2}{\gamma}$, V is volume, and T is temperature (Wang, 2017).

To improve the optimal feature of the PA signal, the duration of pulsed laser light radiation (τ) must be a few nanoseconds to include the following two conditions:

- thermal confinement, which represents the neglect of thermal diffusion during laser light irradiation (Li, Wang, 2009):

$$\tau < \tau_{th} = \frac{d_c^2}{4D_T}, \tag{4}$$

  where τ_{th} is the thermal confinement threshold, D_T is the thermal diffusivity, and d_c is the desired special resolution;
- stress confinement means neglecting the volume expansion of the absorber during laser light irradiation:

$$\tau < \tau_{st} = \frac{d_c}{V_S}, \tag{5}$$

  where τ_{st} is the stress confinement threshold and V_S is the speed of sound.

Under two conditions, irradiation time can be treated as a delta function (Li, Wang, 2009).

Therefore, we are able to rewrite Eq. (3) in this form:

$$\left[\nabla^2 - \frac{1}{v_s^2}\frac{\partial^2}{\partial t^2}\right]p(r,t) = -\frac{p_0}{v_s^2}\frac{\partial\delta(t)}{\partial t}. \tag{6}$$

The acoustic wave $p(r,t)$ at the position (r) and time (t), prompted by an initial source, $p_0(r) = \Gamma(r)A_e(r)$, where $A_e(r)$ is a spatial electromagnetic (EM) absorption function and $\Gamma(r) = v_s^2\beta/C_p$ is the Grüneisen parameter (Wang, 2017).

2.3. FEM model

2.3.1. Breast model in simulation

Breast tissue consisting of some similar sections is called the lobe, which is made up of many smaller parts called lobules. The milk produced from the lobe is passed to the nipple through tiny vessels named ducts. Fibrous tissue and fat fill the spaces between the lobules and ducts. In addition, fat is present in different regions: subcutaneous, retro-mammary, and intra-glandular. Figure 1 shows a cross-section of the human mammary in detail. Most of the initial development of cancer occurs inside the glandular tissue. Breast cancer can be in either lobes or ducts. Based on the starting location, ductal carcinoma in situ (DCIS) and lobular carcinoma in situ (LCIS) are the two main types of in situ breast cancer (American Cancer Society, 2019). This study aims to model breast tissue in real dimensions for accurate screening of PA signals. In modeling, different parts of the breast tissue are separated to discriminate the distinct characteristics of each part required in the steps of the PA signal propagation.

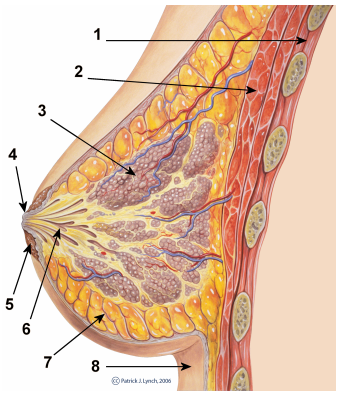

Fig. 1. Cross-sectional image of the normal breast: 1 – chest wall; 2 – pectoralis muscles; 3 – lobules; 4 – nipple; 5 – areola; 6 – milk duct; 7 – fatty tissue; 8 – skin (Lynch, Jaffe, 1987).

The breast has been modeled as a hemisphere with different layers, as shown in Fig. 2. A tumor at a diameter under 20 mm with a spherical shape has been supposed to investigate early-stage cancer (Hammer *et al.*, 2008). Breast tissue is considered as a hemisphere with a diameter of 80 mm. The size of the breast is based on the actual available sizes (Bengtson, Glicksman, 2015). The entire tissue is enclosed inside a semi-ellipsoid chamber of water. The inner layers of breast tissue are simulated as semi-ellipsoid layers consisting of the gland, adipose, and muscle of appropriate size in realistic dimensions. The laser source is located as a point source near tumor side of the breast tissue in the aqueous environment, the distance of laser source to the tissue is about 3 mm in coordinates as follows: $x = 77$ mm, $y = 36$ mm, $z = 53$ mm (Fig. 2b).

a)

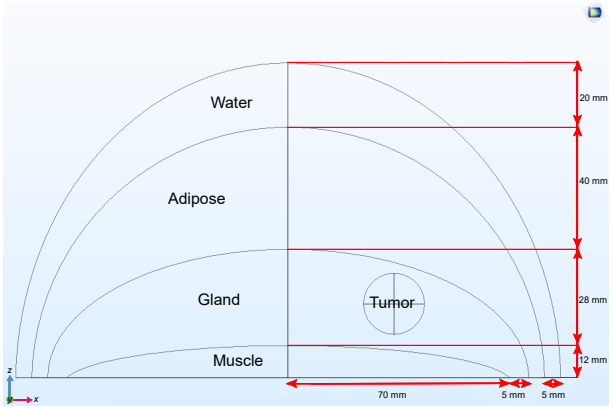

b)

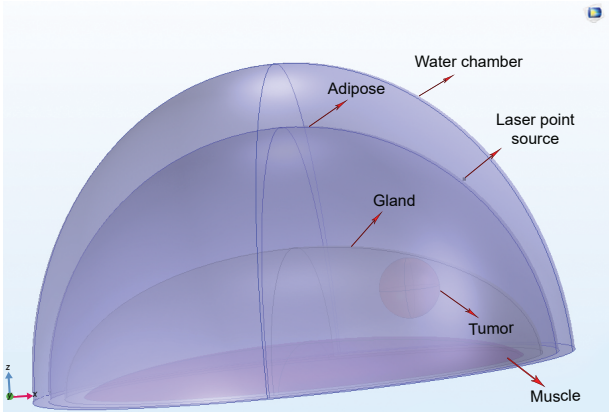

Fig. 2. a) Schematic of the cross-sectional view of the breast model at LOT1 scenario with dimensional details; b) 3D computational domain of breast model in COMSOL Multiphysics.

For a complete study of simulation and subsequently PA signal, we have considered various scenarios for breast tumor, different positions, and sizes, which change in each scenario as abbreviated and listed in Table 1. In all scenarios mentioned, the location and power of the laser light has not changed. Three scenarios for tumor location change were defined: 1) entirely inside the glandular tissue (LOT1); 2) entirely inside the adipose (LOT2); 3) between the gland and adipose (LOT3). Also, compared to the base scenario: (LOT1), in LOT2 and LOT3, the tumor location just along the z-axis increased by 10 and 25 mm, respectively.

Table 1. Various scenarios considered in the simulation.

Scenario name	Location of tumor	Diameter of tumor [mm]
LOT1	Inside gland	19
LOT2	Inside adipose	19
LOT3	Between gland and adipose	19
DOT1	Between gland and adipose	40

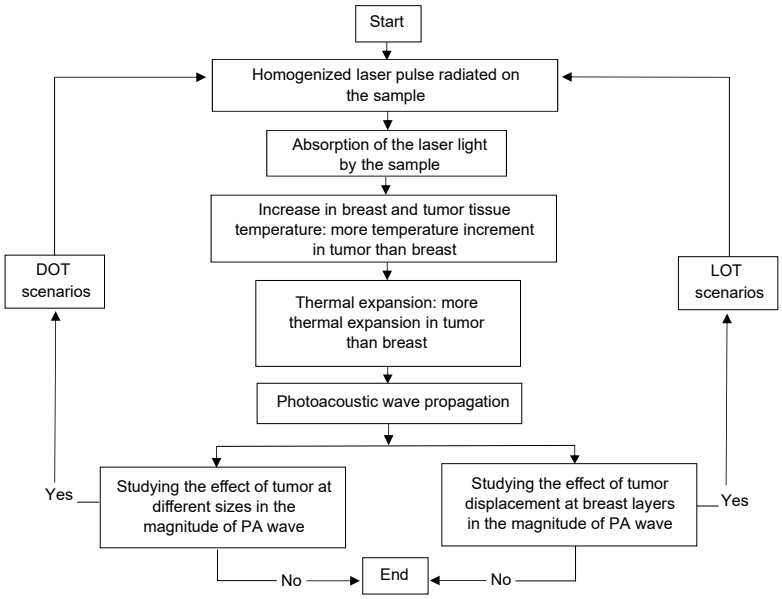

Fig. 3. Flowchart description of the procedure of the PAI and the simulations.

In the scenario of increasing the tumor size (DOT1), the tumor radius compared to previously defined scenarios has increased from 9.5 mm to 20 mm without changing the coordinate position of the tumor. However, due to the increase in tumor diameter, it will be located between adipose tissue and glands. For a better conception of the PAI process and the procedure of the simulations, a schematic flowchart is illustrated in Fig. 3.

We used four modules of COMSOL Multiphysics to simulate PA propagation in the breast. We described all of these in the following.

2.3.2. Light propagation

The initial local acoustic pressure wave (p_0) could also be estimated with the following equation to evaluate the amount of EM energy absorption effectively (Wang, 2017):

$$p_0(r) = \Gamma \eta_{th} \mu_a F, \tag{7}$$

where Γ is the Grüneisen parameter, η_{th} is the percentage of optical absorption that is converted into heat, μ_a is the optical absorption coefficient [cm^{-1}], and F is the optical fluence [J/cm^2]. The optical fluence of radiated laser light is directly related to the amplitude of acoustic pressure waves. Therefore, to obtain a strong PA signal, we must maximize the laser fluence on tissue. In the diffusion regime:

$$F(r) = \frac{F_0}{4\pi D r} e^{-(\mu_{\text{eff}})r}, \tag{8}$$

where r is the distance from the source, F_0 is the fluence at the source, D is the diffusion constant ($D = 1/(3(\mu_a + \mu_s'))$), and $\mu_{\text{eff}} = (\sqrt{\mu_a/D})$ is the effective attenuation coefficient. According to Eq. (8), the penetration depth of the laser is defined by (μ_{eff}) which is dependent on the laser wavelength. In PAI, red, and near-infrared (NIR) wavelengths usually are preferred because, in this wavelength range, the optical attenuation of biological tissue is at its lowest level. HbO_2, HHb, and water are assumed to be the main absorbers in this study. In particular, a wavelength of around 800 nm is the isosbestic point of the molar extinction spectra of HbO_2 and HHb (Wang, 2017). Here, we modeled a radiated laser source as the Gaussian pulse in the 800 nm wavelength, with power, $W_p = 8$ mJ/cm^2, pulse duration $\tau_p = 10$ ns, and $\tau_{\text{center}} = 30$ ns. The radiated laser fluence is modeled by the "coefficient form PDE" interface in COMSOL. The optical properties of the tumor and glandular tissue depend on the assumed magnitude of absorbers that have a dramatic effect at the given wavelength. Once the optical properties are obtained at each wavelength, we can calculate the absorption coefficient of light, μ_a [cm^{-1}], of an absorber by using one of these equations (Jacques, 2013):

$$\mu_a = -\frac{1}{T}\frac{\partial T}{\partial L}, \tag{9}$$

$$T = e^{-\mu_a L} = 10^{-\varepsilon C L} = e^{-4\pi n'' L/\lambda}, \tag{10}$$

where T (dimensionless) is transmitted or surviving fraction of the incident light after an incremental path length ∂L [cm], n'' is the imaginary refractive index of the medium, ε is the extinction coefficient [cm^{-1}M^{-1}], and C(M) is the concentration of chromophore. The absorption coefficient of a tissue is the sum of all main absorbers:

$$\mu_a = \ln(10) \sum_i C_i \varepsilon_i. \tag{11}$$

Table 2. Related parameters of the breast tissue sections and tumor at 800 nm in the first module of COMSOL.

Materials	Density ρ [kg/m^3]	Refractive index	μ_a at 800 nm [mm^{-1}]	μ_s' at 800 nm [mm^{-1}]
Adipose	930 [a, b]	1.455 [c]	0.00193	1.52
Glandular	1050 [a, b]	1.4 [c]	0.00436	1.12
Muscle	1030 [d]	1.4 [d]	0.230 [d]	0.785 [d]
Water	994 [b]	1.3290 [e]	0.00196 [f]	0.0000402 [e, f]
Tumor	1050 [a]	~1.4 [g]	0.00302	0.625

[a](Soltani *et al.*, 2019); [b](Hasgall *et al.*, 2018); [c](Dehghani *et al.*, 2005); [d](Wang *et al.*, 2012); [e](Hale, Querry, 1973; Polyanskiy, 2016); [f](Downing, 2008); [g](Metwally *et al.*, 2014).

Table 3. Required parameters in the "bioheat transfer" module.

Materials	Thermal conductivity k [W·m^{-1}·k^{-1}]	Specific heat capacity C_p [J·kg^{-1}·K^{-1}]	Coefficient of thermal expansion β [K^{-1}]
Adipose	0.21 [a]	2770 [a]	3E-5 [a]
Glandular	0.48 [a]	3770 [a]	4.5E-5 [a]
Muscle	0.49 [b]	3421 [b]	26.73E-5 [c]
Water	0.60 [d]	4178 [d]	~24E-5 [e]
Tumor	0.54 [a]	3852 [a]	6.5E-5 [a]

[a](Soltani *et al.*, 2019); [b](Singh, Repaka, 2018); [c](Wilkie, 1953, Lan *et al.*, 2019); [d](Hasgall *et al.*, 2018); [e](Oraevsky *et al.*, 2001).

Also, the reduced scattering (or transport scattering) coefficient of light, μ_s' [mm^{-1}], the spectrum of tissue has been shown to fit well to an empirical approximation to the Mie scattering theory given by (Dehghani *et al.*, 2009):

$$\mu_s' = a\lambda^{-b}, \tag{12}$$

where a and b are the scatter amplitude and the scatter power, respectively, at any wavelength in µm.

The percentage of absorbent ingredients of tumor, glandular tissue, and adipose of breast is based on (Dehghani *et al.*, 2009). The spectral characteristics of HHb, HbO_2, and water at 800 nm are taken from references (Hale, Querry, 1973; Prahl, 2017). The optical parameters of breast tissue sections and tumor used in "coefficient form PDE" module at COMSOL are listed in Table 2.

We entered the effect of radiant laser light as a point source in the finite element-based numerical model irradiated onto breast tissue surrounded by an aqueous medium. The boundary conditions are also based on references (Wang *et al.*, 2012).

2.3.3. Heat transfer

The second part of the acoustic pressure wave production in the PA phenomenon process is converting the penetrating energy of the radiant laser into heat of which the tumor will have the highest absorption amount according to its material properties. This part can be described by the "bioheat transfer" module of COMSOL. We can connect this module by the heat source that can be inserted in an equation by multiplying the optical absorption coefficient and the optical fluence rate estimated previously. The required thermal properties of breast tissue and tumor used in the heat transfer module are listed in Table 3.

2.3.4. Thermal expansion

Due to the increase in tumor temperature, the tumor subsequently undergoes thermoelastic expansion, which was modeled using a "structural mechanics" module. All related parameters entered in this module are listed in Table 4.

Table 4. Related parameters in the "structural mechanics" module.

Materials	Poisson's ratio
Adipose	0.49 [a]
Glandular	0.49 [a]
Muscle	0.45 [b]
Water	0.4995 [c]
Tumor	0.49 [d]

[a](Bhatti, Sridhar-Keralapura, 2012; Gefen *et al.*, 2007; Soltani *et al.*, 2019); [b](Grimal *et al.*, 2005); [c](Gefen *et al.*, 2007); [d](Soltani *et al.*, 2019).

2.3.5. PA signal generation

Finally, the pressure wave propagation can be studied using the "pressure acoustics, transient" module in COMSOL. Table 5 lists all related parameters in the module of this section.

Table 5. All related parameters in the last module of COMSOL.

Materials	Speed of sound C_s [m/s]	Young's modulus [Pa]
Adipose	1440.2 [a]	18E3 [b]
Glandular	1505.0 [a]	50E3 [b]
Muscle	1588.4 [a]	675E3 [c]
Water	1482.3 [a]	Bulk modulus = 2.1790576 GPa [d]
Tumor	1540 [e]	106E3 [b]

[a](Hasgall *et al.*, 2018); [b](Soltani *et al.*, 2019); [c](Grimal *et al.*, 2005); [d](Zhutovsky, Kovler, 2015); [e](Li *et al.*, 2009).

2.3.6. Image reconstruction

In this section, we describe the algorithm used in the image reconstruction section. There are various algorithms and their reformation for reconstruction of a proper image such as universal back-projection, time reversal, etc. (Dobrucki, Opieliński, 2000; Tasinkevych *et al.*, 2018, Wang, 2017). For PAI reconstruction, a phase-controlled algorithm was used in this study. For each reconstructed pixel in the image, $P_{\mathbf{m}}$, we have the following formula (Zhou *et al.*, 2011):

$$P_{\mathbf{m}} = \sum_{k=1}^{K} D(\theta)_k P(t_{mk}), \tag{13}$$

where $\mathbf{m}$ is the spatial vector of the PA source, k is the position of the k-th detector, and K is the total number of working detectors, $D(\theta)$ is defined as the projection intensity weight function of θ, the projection angle which is no more than the maximal acceptance angle of the array element, $P(t_{mk})$ is the signal value collected by the k-th detector at position $\mathbf{m}$. The t_{mk} represents the time when PA pulses spread from position $\mathbf{m}$ to k. The r_{mk} is the distance between the PA source at position $\mathbf{m}$ and the k-th detector. The v is the average velocity of the acoustic wave in tissue. According to Eq. (13), the volumetric data collected by the plane transducer array in a single laser pulse can be used to reconstruct 2D projection image slices at various z-axis depths. To have the final 3D image of the breast, proper processing software could merge these slices.

3. Results and discussion

Using the finite element (FE) based simulation models, light propagation, absorption, conversion to heat, PA wave formation from the target (tumor), and its propagation in breast tissue were successfully simulated. For a better demonstration of our simulation process, captured PA signals in the L1 model of COMSOL simulation have been converted to 2D tomography image slices using MATLAB code. For 3D data visualization, processing, and analysis we can convert these slices to 3D images using special software. Converting 2D image slices to 3D breast tissue have not been done by the relevant software in this project. Finally, comparative results of all simulations concerning the tumor location and size were studied in detail.

3.1. Simulation model in detail

A laser source as the Gaussian pulse radiated on tissue as a point source is showed in Fig. 4. The coordinates and geometric position of discussed points in this section are shown in Fig. 5. We have chosen 6 points, two points inside and outside of the tumor near the wall to study the accuracy of the tumor edge detection in our PAI simulation, a point inside the adipose region, a point in the glandular region, and the two other points inside the tumor on the other axis for studying stress.

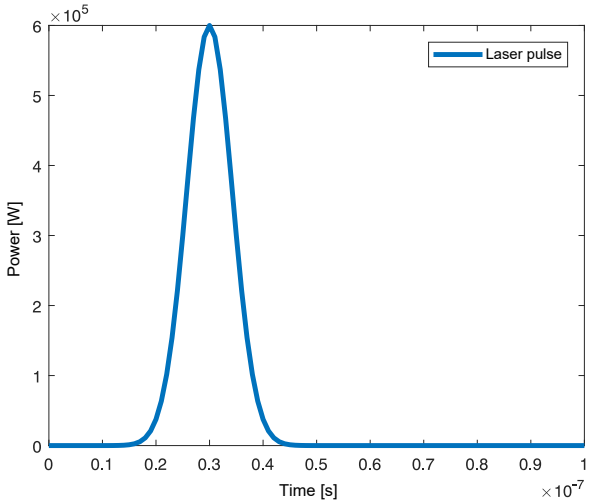

Fig. 4. Function diagram of laser pulse radiated as a point source on tissue, with power W_p = 8 mJ/cm^2, pulse duration τ_p = 10 ns, and τ_{center} = 30 ns.

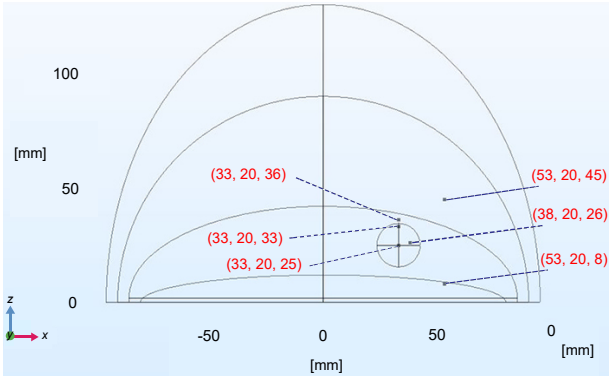

Fig. 5. Coordinate location of points mentioned in simulation studies.

The radiated laser fluence shown in Fig. 6, represents the laser fluence variation in time at four points

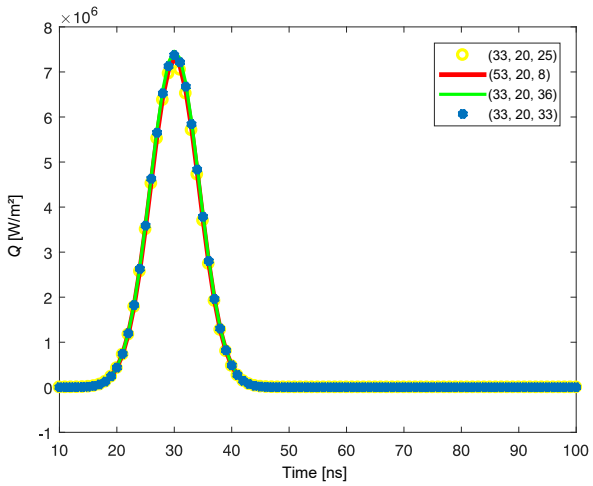

Fig. 6. Radiated laser fluence of four points: inside and outside the tumor close to the wall, center of the tumor and inside a muscle layer, in the L1 simulation model.

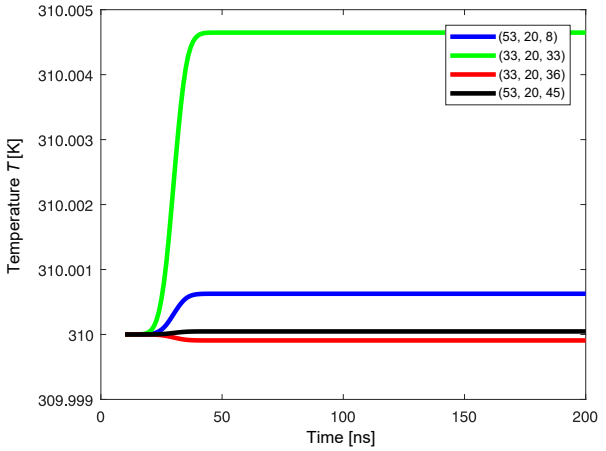

Fig. 7. Temperature changes in Kelvin, four points: inside and outside the tumor, one in glandular and the other in the adipose regions according to time variables.

of interest. The next step is converting the effect of laser light to heat and studying the behavior of tissues and tumors.

The temperature variations of four points are selected as representative of four places: inside and outside the tumor, near the wall of the tumor to determine the accuracy of detecting the edges of the tumor, a point in the muscular region, and a point in the glandular region. These are shown in Fig. 7. As is shown in Fig. 7, due to the amount of absorption of the laser energy, the temperature change of points is different, it is greater for the point inside the tumor and depends on the different optical and thermal characteristics of the tumor (all these specifications are listed in Tables 1 and 2) compared to breast tissue. The increase in temperature inside the tumor is approximately 0.0046 degrees in Kelvin, while the temperature of the study points slightly outside the tumor wall and in the adipose region has not changed much. Due to muscle tissue's thermal and optical characteristics, a slight increase in temperature is observed at the point located in this section, which can be ignored according to the increased value in the tumor temperature. In all calculations, the human body temperature, 310 degrees in Kelvin, is considered.

For further clarity on temperature changes in tissue and tumor, a cut surface was considered in the z–y coordinate plane passing through the center of the tumor in x coordinate (x = 33). Figure 8 indicates an increase in a temperature gradient in the tumor region compared to other parts of the tissue at time = 30 ns. High levels of the laser light absorption by the tumor tissue and its conversion to heat are the reason for the increase in heat of tumor tissue compared to other parts of breast tissue.

Increasing the temperature of the tumor compared to other parts of the tissue will cause the tumor tis-

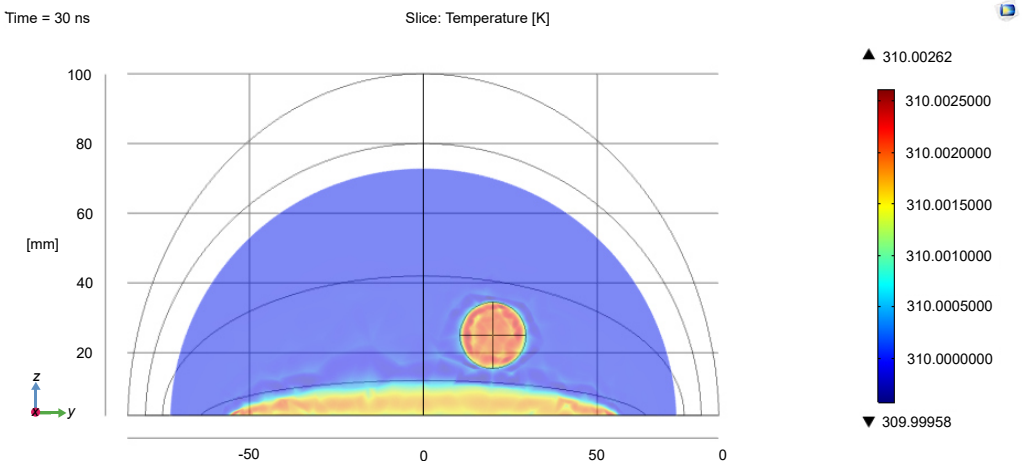

Fig. 8. Temperature gradient distribution of breast and tumor tissues on cut surfaces in the z–y plane at x = 33 mm and t = 30 ns.

sue to expand. Figure 9 shows the internal expansion changes of the three internal points of the tumor. The increase in the internal expansion of the tumor is about 3 N/m^2.

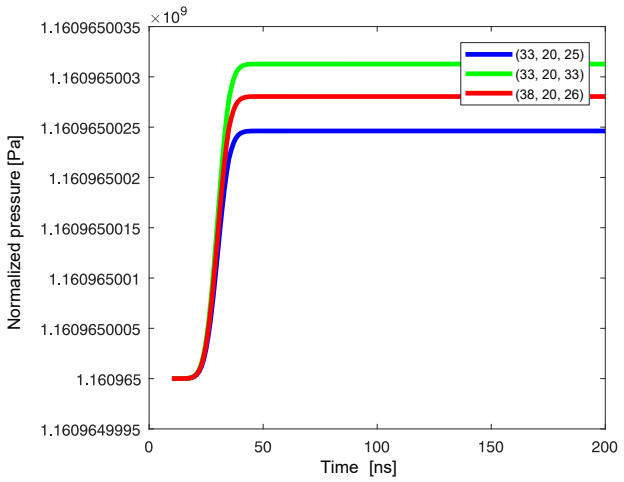

Fig. 9. Internal expansion changes of the three internal points of the tumor.

Expansion changes inside the tumor will cause an acoustic wave inside the tumor tissue and propagate it into the breast tissue. In the latest module of COMSOL, we have studied the propagation of acoustic pressure waves around tumor tissue. The images of the acoustic pressure wave propagation gradient in the surface z–y at x = 33 mm are shown in Fig. 10 in two steps and times as the first cycle of acoustic wave propagation.

The last step is to transfer information obtained from COMSOL simulation to MATLAB software and reconstruct the 2D tomographic image slices. The sensor's data that contain ultrasonic wave information are defined as "Domain Point Probe" in COMSOL, and 32 number of these "Domain Point Probes", according to previous statements, are located around the breast cup on the arc of 2D tomographic slices. Fifteen 2D tomographic slices of breast tissue have been considered according to Fig. 11, while these slices cutting the breast tissue Perpendicular to the x-axis, are located at a distance of about 1 cm from each other. Each "Domain Point Probe" information is exported from COMSOL as a matrix whose dimension depends on the simulation time and number of sensors.

The exported matrices are to be used for subsequent processing in MATLAB. The data of four sensors is simply drawn in Fig. 12.

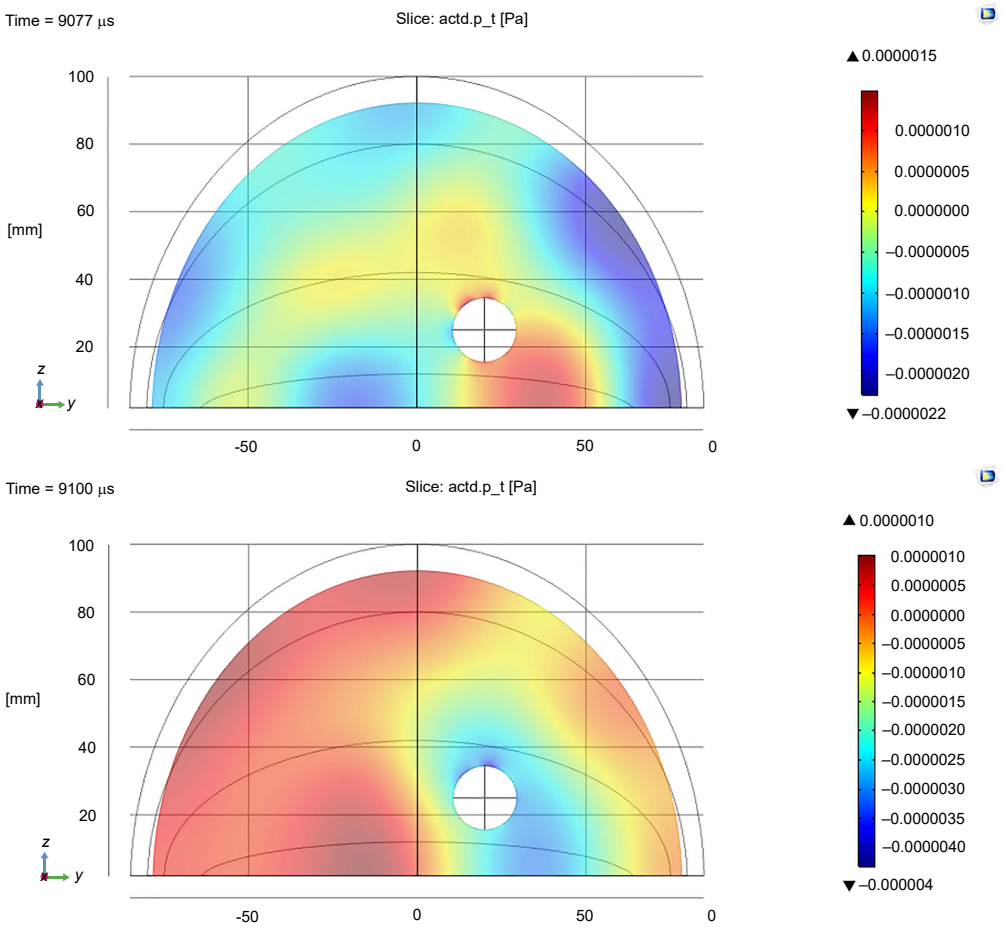

Fig. 10. Acoustic pressure wave gradient distribution at two steps and times on cut surfaces in the z–y plane at x = 33 mm.

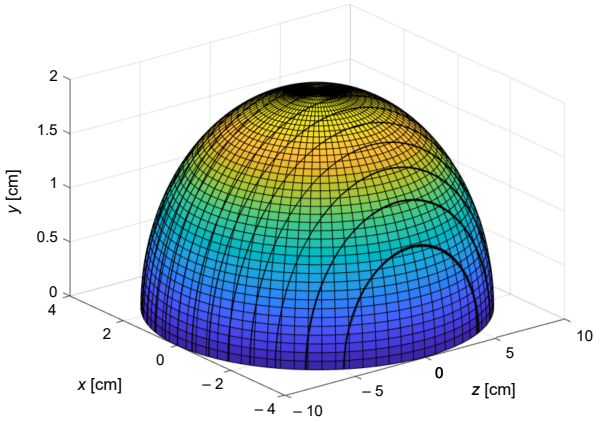

Fig. 11. Fifteen 2D tomographic slices of breast tissue used in this simulation.

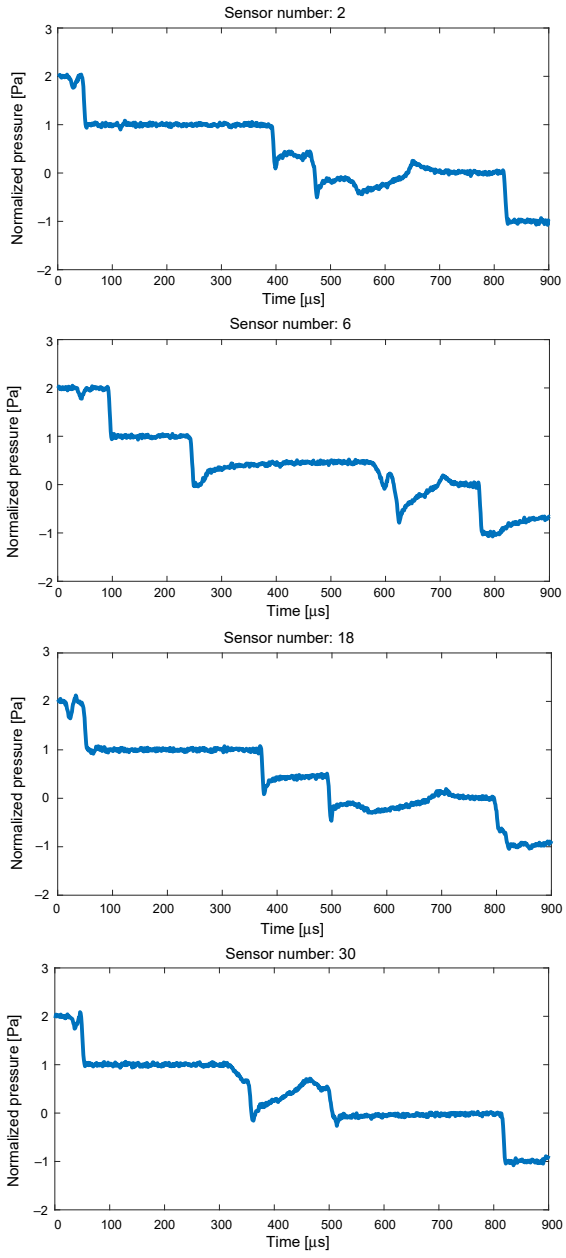

Fig. 12. Simple plotting of four ultrasonic sensors data.

2D tomographic reconstructed image slices for 3D image creation should be repeated in different coordinates; here we just showed two slices in Fig. 13: a cut surface, the y–z surface, at x = 33 mm and x = 37 mm. MATLAB code results for the reconstruction took a 1 minute processing. Finally, by Amira (version 5.5, TGS Template Graphics Software) software, we could visualize these 2D reconstructed slices to 3D, for operator of device, but here for our analyzing the 2D slices and sensor's data are adequate.

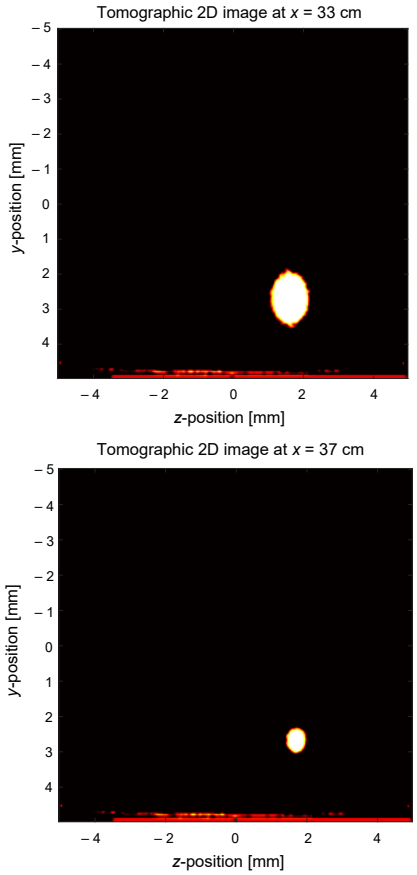

Fig. 13. 2D tomographic image in one slice of simulation, derived from MATLAB code, at x = 33 mm and x = 37 mm.

According to the anatomy of the breast tissue, the muscle layer is at the junction of the breast tissue with the chest wall, and due to the proximity of the characteristics of muscle and tumor, a certain error in image reconstruction is shown. This error could be easily removed based on the fixed location of the muscle and its specific shape and brightness.

3.2. Effect of tumor location

According to Table 1 and the different scenarios we have considered for the tumor location and size, in this section, we study the changes in temperature and intensity of the emitted pressure wave based on the change in the tumor location compared to the LOT1 mode.

According to the chart in Fig. 14 and the values of temperature changes for the tumor in different places, it was observed that for the case where the tumor was located in the adipose tissue, the absorption of radiant laser energy by the tumor would be higher than others; consequently, temperature changes were high.

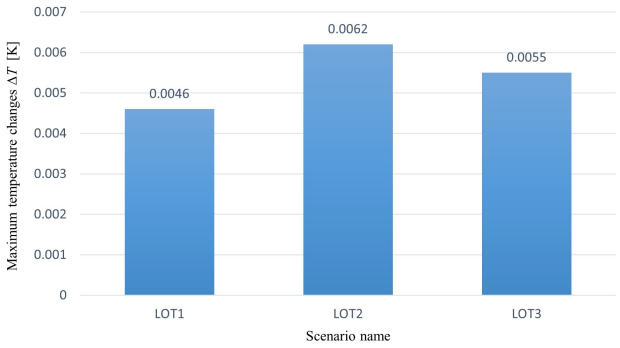

Fig. 14. Temperature changes based on different scenarios.

Based on the chart in Fig. 15, the amount of pressure change created in the tumor located in the adipose tissue is also high. This is because of the large difference in optical and thermal properties between the tumor tissue and the adipose tissue. By studying the tissue property tables (Tables 2 to 4), the cause can be observed.

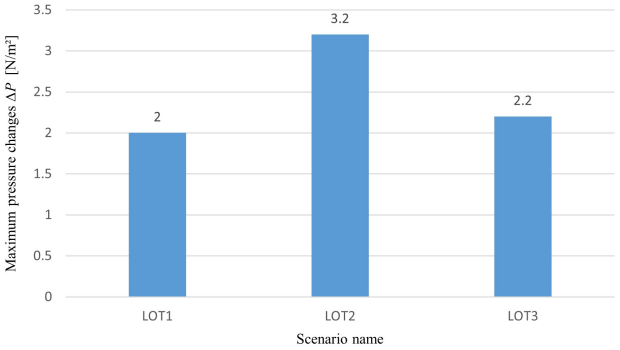

Fig. 15. Pressure changes based on different scenarios.

Increasing the temperature and pressure changes will cause the acoustic pressure wave to propagate more intensely, resulting in more accurate and easier tumor detection.

The final result of our study for the tumor location in different layers of breast tissue is completely consistent with the results of breast imaging by the thermoacoustic method (Soltani *et al.*, 2019). In both methods, the tumor placement in the adipose tissue results in a strong PA wave. In other words, it would be easier to diagnose a tumor that is located in the adipose section compared to other layers.

3.3. Effect of tumor size

To study the effect of increasing the diameter of the tumor, two scenarios have been considered: one with a diameter of 19 mm (LOT1); the other with 40 mm (DOT1). The choice of a tumor with a diameter of less than 2 cm is to evaluate the ability of PAI to detect the tumor in the early stages (Hammer *et al.*, 2008).

Based on the charts in Figs. 16 and 17, which show a comparison of the increase in temperature and pressure changes in the two scenarios respectively, it is obvious that the magnitude of the temperature change of a large-diameter tumor is greater than that in a small-diameter tumor.

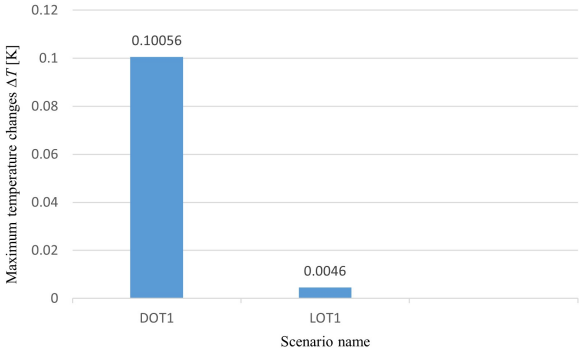

Fig. 16. Temperature changes based on different scenarios.

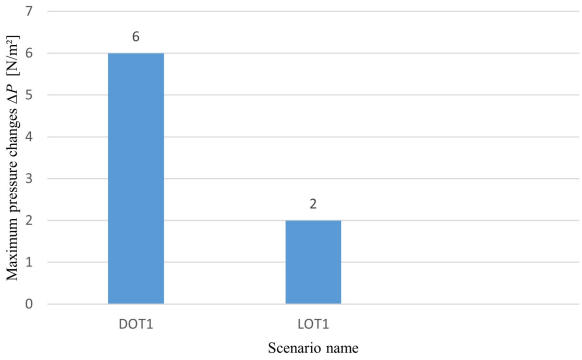

Fig. 17. Pressure changes based on different scenarios.

The reason for this is obvious. As the size of the tumor increases, the amount of energy absorbed by the radiant laser light will be higher. Compared to the thermoacoustic method (Soltani *et al.*, 2019), our results also indicate that the amplitude of the PA wave will increase with increasing tumor diameter.

4. Conclusions

In this study, breast tissue tomography was simulated using the PA phenomenon in real dimensions and different constituent layers in suitable and efficient software. To select the proper software, various software were examined to select the most suitable option. Attempts were also made to consider the different layers that make up breast tissue and enter all the required specifications in the simulation completely and accurately. In all the stages, the simulation process tried to be as close as possible to the real state to

cite the results of this simulation implementation of the PAI system and evaluate the strengths and weaknesses of the PA breast tissue imaging system. The simulations were performed for four different scenarios based on the size and location of the tumor to investigate the changes in the resulting PA signal in different states. It is possible to define different scenarios. In each scenario, the magnitude of temperature changes and consequently the acoustic pressure magnitude were obtained. Due to the optical, thermal, elastic, and acoustic characteristics of different layers of breast tissue and tumor which show a greater difference between the adipose tissue and the tumor, it was expected that the absorption of radiant laser light will be high if more tumor forms in the adipose layer of breast tissue.

Consequently, temperature changes and the resulting acoustic pressure will have a large amplitude. However, the acoustic pressure magnitude will be the lowest for tumors located in the glandular layer and make diagnosis more difficult. Also, by examining the simulation for a tumor with a larger diameter and the consequent increase in the acoustic pressure amplitude, it is quite clear that large tumors can easily be identified. But due to the capability of the PA phenomenon and incorporation of optical and ultrasound imaging advantages, it was able to detect tumors smaller than 2 cm in size so that cancerous tumor tissue could be detected in early stages.

Acknowledgments

We wish to thank Duckman Proofreading for the English language editing. The author acknowledges the usage of the COMSOL Multiphysics® software version 5.4 for Linux at a data processing center of the Sahand University of Technology, Tabriz, Iran.

Data availability

The data that support the findings of this study are available from the corresponding author upon reasonable request.

References

1. Ai M., Shu W., Salcudean T., Rohling R., Abolmaesumi P., Tang S. (2017), Design of high energy laser pulse delivery in a multimode fiber for photoacoustic tomography, *Optics Express*, **25**(15): 17713–17726, doi: 10.1364/OE.25.017713.

2. Akhlaghi N., Pfefer T.J., Wear K.A., Garra B.S., Vogt W.C. (2019), Multidomain computational modeling of photoacoustic imaging: Verification, validation, and image quality prediction, *Journal of Biomedical Optics*, **24**(12): 121910, doi: 10.1117/1.JBO.24.12.121910.

3. American Cancer Society (2019), Breast cancer facts & figures 2019–2020, *American Cancer Society, Inc.*, https://www.cancer.org/content/dam/cancer-org/research/cancer-facts-and-statistics/breast-cancer-facts-and-figures/breast-cancer-facts-and-figures-2019-2020.pdf.

4. Bengtson B.P., Glicksman C.A. (2015), The standardization of bra cup measurements: Redefining bra sizing language, *Clinics in Plastic Surgery*, **42**(4): 405–411, doi: 10.1016/j.cps.2015.06.002.

5. Bhatti S.N., Sridhar-Keralapura M. (2012), A novel breast software phantom for biomechanical modeling of elastography, *Medical Physics*, **39**(4): 1748–1768, doi: 10.1118/1.3690467.

6. Boppart S.A., Luo W., Marks D.L., Singletary K.W. (2004), Optical coherence tomography: feasibility for basic research and image-guided surgery of breast cancer, *Breast Cancer Research and Treatment*, **84**(2): 85–97, doi: 10.1023/B:BREA.0000018401.13609.54.

7. Cassidy J., Nouri A., Betz V., Lilge L. (2018), High-performance, robustly verified Monte Carlo simulation with FullMonte, *Journal of Biomedical Optics*, **23**(8): 085001, doi: 10.1117/1.JBO.23.8.085001.

8. Corlu A. *et al.* (2007), Three-dimensional in vivo fluorescence diffuse optical tomography of breast cancer in humans, *Optics Express*, **15**(11): 6696–6716, doi: 10.1364/OE.15.006696.

9. Dehghani H., Brooksby B.A., Pogue B.W., Paulsen K.D. (2005), Effects of refractive index on near-infrared tomography of the breast, *Applied Optics*, **44**(10): 1870–1878, doi: 10.1364/AO.44.001870.

10. Dehghani H. *et al.* (2009), Near infrared optical tomography using NIRFAST: Algorithm for numerical model and image reconstruction, *Communications in Numerical Methods in Engineering*, **25**(6): 711–732, doi: 10.1002/cnm.1162.

11. Dobrucki A.B., Opieliński K.J. (2000), Adaptation of image reconstruction algorithm for purposes of ultrasound transmission tomography (UTT), *Archives of Acoustics*, **25**(4): 395–422.

12. Downing J. (2008), Effects of light absorption and scattering in water samples on OBS measurements, *Campbell Scientific, Inc.*, pp. 1–4.

13. Gefen A., Dilmoney B. (2007), Mechanics of the normal woman's breast, *Technology and Health Care,* **15**(4): 259–271, doi: 10.3233/THC-2007-15404.

14. Grimal Q., Naïli S., Watzky A. (2005), A high-frequency lung injury mechanism in blunt thoracic impact, *Journal of Biomechanics*, **38**(6): 1247–1254, doi: 10.1016/j.jbiomech.2004.06.010.

15. Hale G.M., Querry M.R. (1973), Optical constants of water in the 200-nm to 200-μm wavelength region,

Applied Optics, **12**(3): 555–563, doi: 10.1364/AO.12.000555.

16. Hammer C., Fanning A., Crowe J. (2008), Overview of breast cancer staging and surgical treatment options, *Cleveland Clinic Journal of Medicine*, **75**: S10–S16, doi: 10.3949/ccjm.75.Suppl_1.S10.

17. Hasgall P.A. *et al.* (2018), IT'IS Database for thermal and electromagnetic parameters of biological tissues, Version 4.0, *IT'IS Foundation*, doi: 10.13099/VIP21000-04-0.

18. Jacques S.L. (2013), Optical properties of biological tissues: A review, *Physics in Medicine & Biology*, **58**(11): R37, doi: 10.1088/0031-9155/58/11/R37.

19. Jacques S.L., Wang L. (1995), Monte Carlo modeling of light transport in tissues, [in:] *Optical-Thermal Response of Laser-Irradiated Tissue*, Welch A.J., van Gemert M. [Eds.], pp. 73–100, Springer, Boston, MA, doi: 10.1007/978-1-4757-6092-7_4.

20. Lan H., Duan T., Jiang D., Zhong H., Zhou M., Gao F. (2019), Dual-contrast nonlinear photoacoustic sensing and imaging based on single high-repetition-rate pulsed laser, [in:] *IEEE Sensors Journal*, **19**(14): 5559–5565, doi: 10.1109/JSEN.2019.2902849.

21. Laufer J., Elwell C., Delpy D., Beard P. (2006), Absolute measurements of local chromophore concentrations using pulsed photoacoustic spectroscopy, [in:] *Photons Plus Ultrasound: Imaging and Sensing 2006: The Seventh Conference on Biomedical Thermoacoustics, Optoacoustics, and Acousto-optics*, Vol. 6086, pp. 398–405, doi: 10.1117/12.657372.

22. Li C., Duric N., Littrup P., Huang L. (2009), In vivo breast sound-speed imaging with ultrasound tomography, *Ultrasound in Medicine & Biology*, **35**(10): 1615–1628, doi: 10.1016/j.ultrasmedbio.2009.05.011.

23. Li C., Wang L.V. (2009), Photoacoustic tomography and sensing in biomedicine, *Physics in Medicine & Biology*, **54**(19): R59, doi: 10.1088/0031-9155/54/19/R01.

24. Lin L. *et al.* (2018), Single-breath-hold photoacoustic computed tomography of the breast, Nature communications, **9**(1): 2352, doi: 10.1038/s41467-018-04576-z.

25. Lynch P.J., Jaffe C.C. (1987), Generated for multimedia teaching projects by the Yale University School of Medicine, *Center for Advanced Instructional Media.*

26. Metwally M.K. *et al.* (2014), Influence of optical fluence distribution on photoacoustic imaging, *International Journal of Mathematical, Computational, Physical, Electrical and Computer Engineering*, **8**(8): 1108–1112.

27. Oraevsky A.A., Karabutov A.A., Savateeva E.V. (2001), Enhancement of optoacoustic tissue contrast with absorbing nanoparticles, [in:] *Hybrid and Novel Imaging and New Optical Instrumentation for Biomedical Applications*, Vol. 4434, pp. 60–69, doi: 10.1117/12.446693.

28. Pogorzelski S.J., Szurkowski J., Śliwiński A. (1999), Detection of micellar structures in oil-water-surfactant systems with a photoacoustic method, *Archives of Acoustics*, **24**(3): 319–330.

29. Polyanskiy M.N. (2016), Refractive index database (access: 2020).

30. Ponikwicki N. *et al.* (2019), Photoacoustic method as a tool for analysis of concentration-dependent thermal effusivity in a mixture of methyl alcohol and water, *Archives of Acoustics*, **44**(1): 153–160, doi: 10.24425/aoa.2019.126361.

31. Prahl S. (2017), *Assorted Spectra* (assess: 2020).

32. Silverman R.H. *et al.* (2010), High-resolution photoacoustic imaging of ocular tissues, *Ultrasound in Medicine & Biology,* **36**(5): 733–742, doi: 10.1016/j.ultrasmedbio.2010.02.006.

33. Singh S., Repaka R. (2018), Numerical investigation of convective cooling in minimizing skin burns during radiofrequency ablation of breast tumor, *Sādhanā*, **43**(90): 1–8, doi: 10.1007/s12046-018-0872-4.

34. Soltani, M., Rahpeima R., Kashkooli F.M. (2019), Breast cancer diagnosis with a microwave thermoacoustic imaging technique – a numerical approach, *Medical & Biological Engineering & Computing*, **57**(7): 1497–1513, doi: 10.1007/s11517-019-01961-8.

35. Sowmiya C., Thittai A.K. (2017), Simulation of photoacoustic tomography (PAT) system in COMSOL and comparison of two popular reconstruction techniques, [in:] *Medical Imaging 2017: Biomedical Applications in Molecular, Structural, and Functional Imaging*, **10137**: 435–445, doi: 10.1117/12.2254450.

36. Tasinkevych Y., Lewandowski M., Klimonda Z., Walczak M. (2018), Synthetic aperture cardiac imaging with reduced number of acquisition channels. A feasibility study, *Archives of Acoustics*, **43**(3): 437–446, doi: 10.24425/123915.

37. Treeby B.E., Cox B.J., (2010), k-Wave: MATLAB toolbox for the simulation and reconstruction of photoacoustic wave fields, *Journal of Biomedical Optics*, **15**(2): 021314, doi: 10.1117/1.3360308.

38. Wang L., Jacques S.L. (1992), *Monte Carlo Modeling of Light Transport in Multi-Layered Tissues in Standard C.*, University of Texas, MD Anderson Cancer Center.

39. Wang L.V. [Ed.] (2017), *Photoacoustic Imaging and Spectroscopy,* CRC Press.

40. Wang L.V. (2004), Ultrasound-mediated biophotonic imaging: A review of acousto-optical tomography and photo-acoustic tomography, *Disease Markers*, **19**(2–3): 123–138, doi: 10.1155/2004/478079.

41. Wang L.V. (2008), Prospects of photoacoustic tomography, *Medical Physics*, **35**(12): 5758–5767, doi: 10.1118/1.3013698.

42. Wang Z., Ha S., Kim K. (2012), Evaluation of finite-element-based simulation model of photoacoustics in biological tissues, [in:] *Medical Imaging 2012: Ultrasonic Imaging, Tomography, and Therapy*, **8320**: 470–478, doi: 10.1117/12.912152.

43. Wilkie D.R. (1953), The coefficient of expansion of muscle, *The Journal of Physiology*, **119**(4): 369–375, doi: 10.1113/jphysiol.1953.sp004852.

44. Zho Q., Ji X., Xing D. (2011), Full-field 3D photoacoustic imaging based on plane transducer array and spatial phase-controlled algorithm, *Medical Physics*, **38**(3): 1561–1566, doi: 10.1118/1.3555036.

45. Zhutovsky S., Kovler K. (2015), Evaluation of the thermal expansion coefficient using non-destructive testing, [in:] *Proceedings of 110th International Conference on Mechanics and Physics of Creep, Shrinkage, and Durability of Concrete and Concrete Structures, CONCREEP*, **10**: 1137–1146, doi: 10.1061/9780784479346.136.